

## OPTICAL FIBER EXTRINSIC MICRO-CAVITY SCANNING MICROSCOPY

A. Di Donato<sup>\*</sup>, A. Morini, and M. Farina

DII Dipartimento di Ingegneria dell'Informazione, Università Politecnica delle Marche, Ancona 60131, Italy

**Abstract**—An extrinsic Fabry-Perot cavity in optical fiber is used to achieve surface imaging at infrared wavelengths. The micro-cavity is realized by approaching a single mode fiber with a numerical aperture  $NA$  to a sample and it is fed by a low-coherence source. The measurement of the reflected optical intensity provides a map of the sample reflectivity, whereas from the analysis of the reflected spectrum in the time/spatial domain, we disentangle the topography and contrast phase information, in the limit of nearly homogeneous sample with complex permittivity having  $\text{Im}(\varepsilon) \ll \text{Real}(\varepsilon)$ . The transverse resolution is not defined by the numerical aperture  $NA$  of the fiber and consequently by the conventional Rayleigh limit (about  $0.6\lambda/NA$ ), but it is a function of the transverse field behavior of the electromagnetic field inside the micro-cavity. Differently, the resolution in the normal direction is limited mainly by the source bandwidth and demodulation algorithm. The system shows a compact and simple architecture. An analytical model for data interpretation is also introduced.

### 1. INTRODUCTION

Fabry-Perot cavities have always received a great deal of interest in the realization of interferometric sensors due to their high sensitivity, simple structure and immunity to electromagnetic interference [1–7]. In recent works, Fabry-Perot micro-cavities were applied to measure the refractive index of optical glasses [8], or to realize wide-range displacement sensors with sub-nanometer resolution for Confocal Laser Microscopy [9]. Thanks to their capability to be integrated in different sub-systems, they have allowed the design of miniaturized multi-cavity biosensors in the study of self-assembled thin-film layers [10].

---

*Received 25 July 2012, Accepted 21 September 2012, Scheduled 26 October 2012*

\* Corresponding author: Andrea Di Donato (a.didonato@univpm.it).

In addition, the widespread use in the field of scanning probe microscopy, as sensors of micro-cantilever displacement, has led to an improvement in the electromagnetic analysis of the cavity behavior in presence of multi reflections, angular misalignments or highly reflective surfaces [11]. As a matter of fact, recent works [12] have been reported analytical models describing the asymmetrical spectral response, the sensitivity, the fringe contrast and the dynamic range of low-coherence interferometers based on fiber Fabry-Perot. In this paper, we describe a scanning probe microscopy technique based on optical fiber micro-cavity, in which a cleaved single mode fiber is approached to a sample. The fiber is used as a probe for image reconstruction. Although this system features some analogies with similar scanning techniques, such as Synthetic Aperture Radars, Spectral Optical Coherence Tomography (OCT) or Scanning Near-Field Optical Microscopy (SNOM) [13,14], it has some aspects that distinguish it from these. In SNOM microscopy, for example, the images are acquired through a tapered fiber optic with sub-wavelength aperture that is placed at nanometer distance over the sample and the interaction is due to near-field emitted from the tip. Differently, in OCT, the optical beam is collimated or focused on a sample through lens. The reflected signal from the surface under investigation interferes with a reference beam. The OCT systems allow to recover the scattering profile, according to models based on the interference of the reference signal with scattered field from the object [14].

In a fiber micro-cavity system, the interaction between the sample and probe occurs at distance of tens of microns whereas a cleaved fiber is used as probe, allowing to work without any lens. With respect to the OCT approach, no reference beam is present and interfering signal directly comes from the micro-cavity in which the diffracted field experiences multiple reflections and interferences. Only in the limit of very low reflective surfaces, the interfering signal can be described by the same analytical model on which are based OCT systems. For this reason, it is not possible for example to apply directly the same algorithm used in OCT to predict the behavior of the micro-cavity response by varying the sample topography or surface refractive index. The same reasoning applies when studying the focusing effect produced through the interference of field diffracted from the fiber facet inside the cavity. The contrast phase images, reflectivity and topographic information can be investigated by means of the optical fiber itself without the use of lens. The absence of lens and bulky components is a factor that allows to realize a compact and mechanically robust architecture, as highlighted in a recent paper [15], where a lens-free holographic microscopy was proposed. Changes of

the surface permittivity and cavity dimensions lead to a variation of the cavity response. The main problem to be addressed in the micro-cavity systems (or interferometers) is the signal demodulation. All the main electromagnetic parameters change periodically making the relation between them and the physical quantity to be measured, non-linear. Many algorithms can be used for the image reconstruction, also borrowed from Spectral Optical Radars, Synthetic Aperture or Ground Penetrating Radars [13, 14, 16]; however they are usually based on models that consider a single scattered wave problem and they cannot be applied directly to the proposed system, due to the presence of multi-reflections inside the cavity. In this work, the spectrum acquired at each point is analyzed in the time domain (which corresponds to a space domain considering the speed of light as known parameter), following a method similar to the one introduced in Scanning Microwave Microscopy [17, 18]. By recording the behavior of the peak of the cavity response in the time domain, we can acquire both topography and contrast phase information. The latter is a function of the effective refractive index of the sample, as well as of the surface topography. The link between these parameters and cavity dimension, together with the sample permittivity, are investigated by means of an analytical model. In addition, for the fiber scanning system, the transverse resolution is not defined by the numerical aperture  $NA$  of the fiber and, consequently, by the conventional Rayleigh limit (about  $0.6\lambda/NA$ ), but it is a function of the transverse field behavior of the electromagnetic field inside the micro-cavity. In fact a small feature of the sample will be detected when its size is of the order of the field dis-homogeneity, not of  $NA$ . Interferences inside the cavity shape the field distribution in the time domain in a such a way that, at a given instant, the incident spot is characterized by a reduced transverse field distribution with respect to the fiber mode diameter. In the following sections it will be described the experimental set-up and how the images are acquired and analyzed, as well as an analytical model of the cavity. Some experimental results are finally reported.

## 2. MODELLING OF OPTICAL MICRO-CAVITY

When the cleaved fiber approaches the sample, a micro-cavity is formed and a spectrum of waves diffracted from the fiber facet interfere after reflecting from the sample surface, giving rise to a stable spectrum and field configuration in the time. A change of cavity dimension and sample permittivity reflects on changes of the cavity time domain response, that can be studied by means of an analytical model. In the following, we will describe the model used

for describing the reflected signal from the cavity and its dependence on the geometrical and dielectric variations. In presence of a low reflectivity surface, the electromagnetic analysis of the optical fiber extrinsic Fabry-Perot cavity can be done approximately by using a two-beam approximation, in which only two interfering beams are considered: i.e., the reflected signal at the fiber interface and back-reflected signal from the external surface [1, 7, 8], while higher order interferences are neglected. Although this approach gives a simple and compact analytical expression for the interference signal that couple-back to the fiber, it does not characterize rigorously the electromagnetic behavior of the cavity, in which a multi-beam interference takes place.

Interference concerns not only the beams generated by multiple reflections at interfaces, but also mutual interference between the plane waves diffracted by the fiber facet. The need for a detailed characterization appears more clearly when the surface is highly reflective, as focused in many papers [12, 19]. The high finesse extrinsic fiber cavities, required in high sensitivity sensor applications, can be analyzed assuming the transfer function of asymmetric F-P cavity with a normal incidence and zero absorption in the mirror and in the medium [8, 9]. The divergence of the beam radiated by the fiber is accounted for through a loss factor, neglecting the mutual interference of the scattered waves. In some works, this approach was improved by introducing the effects of diffracted waves from the fiber and the coupling coefficient between fiber facet and air [1, 11, 12]. In this paper, the response of the extrinsic cavity is derived by applying a continuity condition of the tangential electric and magnetic fields at the interface between cleaved fiber and air gap. Due to symmetry of the fundamental mode and the waveguide geometry, the electromagnetic field at the interface fiber-air is only function of the transverse coordinate  $\mathbf{r}$  and, according to Hankel transformation, it can be de-composed in cylindrical waves [20]:

$$f(\rho) = \int_0^{\infty} H_0(\lambda) J_0(\lambda\rho) \lambda d\lambda \quad H_0(\lambda) = \int_0^{\infty} f(\rho) J_0(\lambda\rho) \rho d\rho \quad (1)$$

with  $J_0$  representing the zero-order Bessel function. The propagation inside a single mode optical fiber can be described with good accuracy through a Linearly Polarized wave with the transverse electric ( $E_x = e_0$ ) and magnetic ( $H_y$ ) fields linked by the admittance  $Y_0(k_r)$  [21]. Imposing tangential field continuity for the electric and magnetic components at interface fiber-air produces:

$$\begin{aligned}
 & \int_0^\infty r(k_r) e(r, k) dk_r + e_0(r, k) (1 + \Gamma_0(k)) \\
 = & \int_0^\infty a(k_r) J_0(k_r r) k_r \left\{ 1 + \Gamma(k_r) e^{-j2\beta(k_r)d} \right\} dk_r \\
 & - \int_0^\infty r(k_r) e(r, k) Y(k_r) dk_r + e_0(r, k) (1 - \Gamma_0(k)) Y_0(k) \\
 = & \int_0^\infty a(k_r) Y(k_r) J_0(k_r r) k_r \left\{ 1 - \Gamma(k_r) e^{-j2\beta(k_r)d} \right\} dk_r \quad (2)
 \end{aligned}$$

In the right-hand term the  $k$ -dependence is neglected whereas the integral covers the whole spectrum of scattered waves that comprises radiated and reactive energies, described by the amplitude  $a(k_r)$ . On the other hand, within the optical waveguide only the guided field is considered for simplicity, neglecting the reflecting continuum spectrum, described by the amplitude  $r(k_r)$  and transverse field distribution  $e(r, k_r)$ . The reflection coefficient  $\Gamma(k_r)$  is a function of the scattered plane waves direction within the cavity, dielectric properties of the medium, transverse dielectric thickness and polarization of diffracted waves. Being the field scattered in the cavity described by an infinite spectrum of cylindrical plane waves, for each plane wave (we assume a fixed polarization along the  $x$  direction, see Fig. 1), the complex

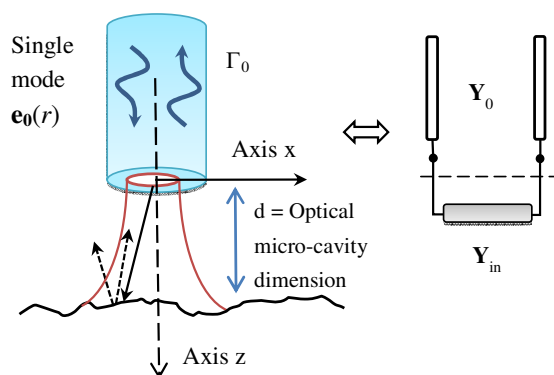


**Figure 1.** Extrinsic fiber optic micro-cavity scheme and equivalent circuit model ( $Y_0$ : admittance of the fundamental mode,  $Y_{in}$ : input admittance).

reflection coefficient can be written as:

$$\Gamma(k_r) = e^{j\alpha(k_r)} = e^{jx-y} \quad \alpha = x + jy \tag{3}$$

in which the term  $y$  is introduced to account for losses introduced by the material. Each cylindrical wave has a different reflection, that can be computed through well know laws of oblique incidence of plane waves on dielectrics [22]. According to (3), the surface scattering effects are neglected. This implies that the model does not consider roughness on sample surfaces [23, 24]. By combining Eqs. (2)–(3), the tangential field continuity can be rewritten as:

$$\begin{aligned} & e_0(r, k) (1 + \Gamma_0(k)) \\ &= \int_0^\infty a(k_r) J_0(k_r r) 2 e^{-j(\beta(k_r)d - \frac{\alpha}{2})} \cos(\varphi(k_r)) k_r dk_r \\ & e_0(r, k) (1 - \Gamma_0(k)) Y_0(k) \\ &= \int_0^\infty a(k_r) Y(k_r) J_0(k_r r) e^{-j(\beta(k_r)d - \frac{\alpha}{2})} (2j) \sin(\varphi(k_r)) k_r dk_r \end{aligned} \tag{4}$$

where the complex number  $\varphi$  is, for each wave, a function of the cavity electrical-length and electromagnetic property of the sample:

$$\varphi = \beta(k_r) d - \frac{\alpha(k_r)}{2}$$

By pre-multiplicating the first equations for  $J_0(k_r r)r$  and exploiting the following orthogonality condition:

$$\int_0^\infty J_0(k_r \rho) J_0(k'_r \rho) \rho d\rho = \frac{\delta(k_r - k'_r)}{k_r} \tag{5}$$

we get the equation:

$$\begin{aligned} & (1 + \Gamma_0(k)) \int_0^\infty e_0(r, k) J_0(k'_r r) r dr \\ &= \int_0^\infty a(k_r) \int_0^\infty J_0(k_r r) J_0(k'_r r) r 2 e^{-j(\beta(k_r)d - \frac{\alpha}{2})} \cos(\varphi(k_r)) k_r dr dk_r \\ & (1 + \Gamma_0(k)) H_0(e_0) = a(k_r) 2 e^{-j(\beta(k_r)d - \frac{\alpha}{2})} \cos(\varphi(k_r)) \end{aligned} \tag{6}$$

On the other hand, the equation related to the magnetic field is pre-multiplicated for  $e_0(r)$   $r$  and integrated in the spatial domain:

$$\begin{aligned}
 (1 - \Gamma_0(k)) Y_0(k) \int_0^\infty e_0(r) e_0(r) r dr &= \int_0^\infty a(k_r) Y(k_r) \int_0^\infty J_0(k_r r) \\
 e_0(r) e^{-j(\beta(k_r)d - \frac{\alpha}{2})} (2j) \sin(\varphi(k_r)) r k_r dr dk_r &(1 - \Gamma_0(k)) Y_0(k) \quad (7) \\
 &= \int_0^\infty a(k_r) Y(k_r) H_0(e_0) e^{-j(\beta(k_r)d - \frac{\alpha}{2})} (2j) \sin(\varphi(k_r)) k_r dk_r
 \end{aligned}$$

The latter is obtained by means of the normalization condition:

$$\int_0^\infty e_0(r) e_0(r) r dr = 1 \quad (8)$$

The ortho-normalization (8) implies that the power carried by the mode is normalized to unity and the field is approximated as Linearly Polarized mode (LP). Continuity of the tangential electric field (6) gives the amplitude of the scattered waves:

$$a(k_r) = \frac{1}{2} (1 + \Gamma_0(k)) H_0(e_0) (1 + j \tan(\varphi(k_r))) \quad (9)$$

whereas by combining Eqs. (6) and (7), we get the expression of the reflected wave:

$$\Gamma_0 = \frac{1 - j \int_0^\infty \frac{\beta(k_r)}{\beta_0} [H_0(e_0)]^2 \tan(\varphi) k_r dk_r}{1 + j \int_0^\infty \frac{\beta(k_r)}{\beta_0} [H_0(e_0)]^2 \tan(\varphi) k_r dk_r} \quad (10)$$

$$Y(k_r) = \frac{\beta(k_r)}{\omega \mu_0} \quad \beta(k_r) = \sqrt{k^2 - k_r^2} \quad \varphi = \beta(k_r) d - \frac{\alpha(k_r)}{2}$$

Above we have also inserted, for the sake of completeness, the relationships defining every quantity. Each scattered wave has an admittance  $Y(k_r)$  and a propagation constant  $\beta(k_r)$ . The normalized input complex admittance:

$$\frac{Y_{in}(k)}{Y_0} = j \int_0^\infty \frac{\beta(k_r)}{\beta_0} [H_0(e_0)]^2 \tan(\varphi) k_r dk_r \quad (11)$$

defines magnitude and phase of the reflected wave, as well as the resonance condition of the cavity.

The presence of a dielectric surface, introduces losses in the optical cavity (even in presence of ideal dielectric) and makes  $\varphi$  a complex term:

$$j \tan(\varphi' + j\varphi'') = \frac{j \tan(\varphi') - \tanh(\varphi'')}{1 - j \tan(\varphi') \tanh(\varphi'')} \quad (12)$$

$$\varphi = \left( \beta(k_r) d - \frac{x(k_r)}{2} \right) - j \frac{y(k_r)}{2}$$

Both real and imaginary part of the complex admittance  $Y_{in}$  are functions of optical cavity and permittivity of the surface under test. A change of the cavity dimension, due to a change in the surface topography height, induces a shift of the resonances frequencies and a contrast variation (see Fig. 2). The same effects appear in presence of a surface permittivity variation in the scanned area. In this case, however, if the medium is homogenous and loss-free, the frequency shifts are less relevant with respect to the contrast variation of the cavity spectrum. In the time domain these changes affect the cavity response and in particular we observe a variation in the peak amplitude and position. The surface imaging is performed by acquiring the changes of these parameters, according to the algorithm described in the next section. The accuracy and the results are strongly dependent on the method used to demodulate the spectrum.

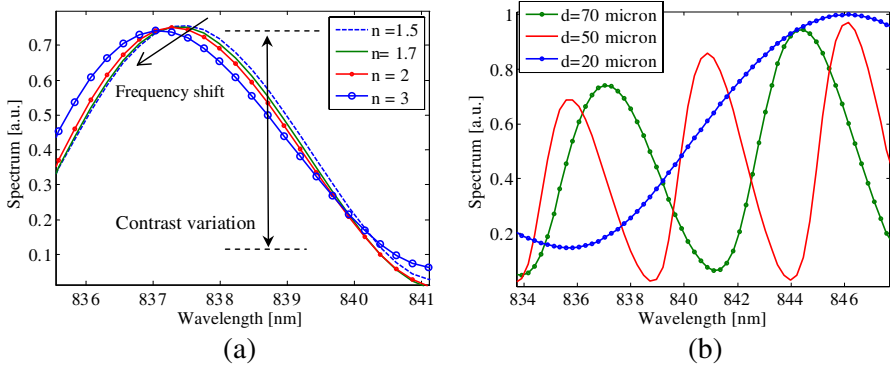
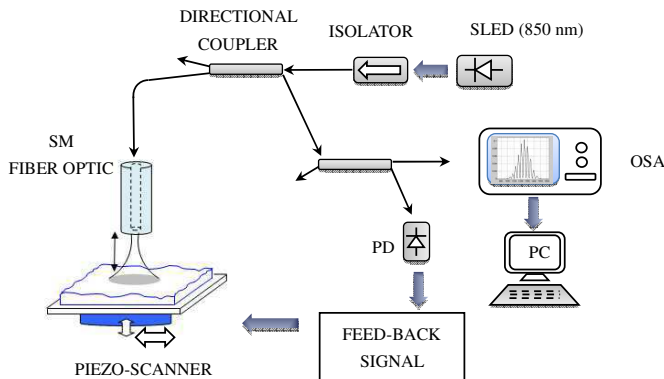


**Figure 2.** Reflected spectrum behavior in presence of (a) sample refractive index changes with a cavity dimension  $d = 50 \mu\text{m}$  and (b) sample-fiber optic distance variations.

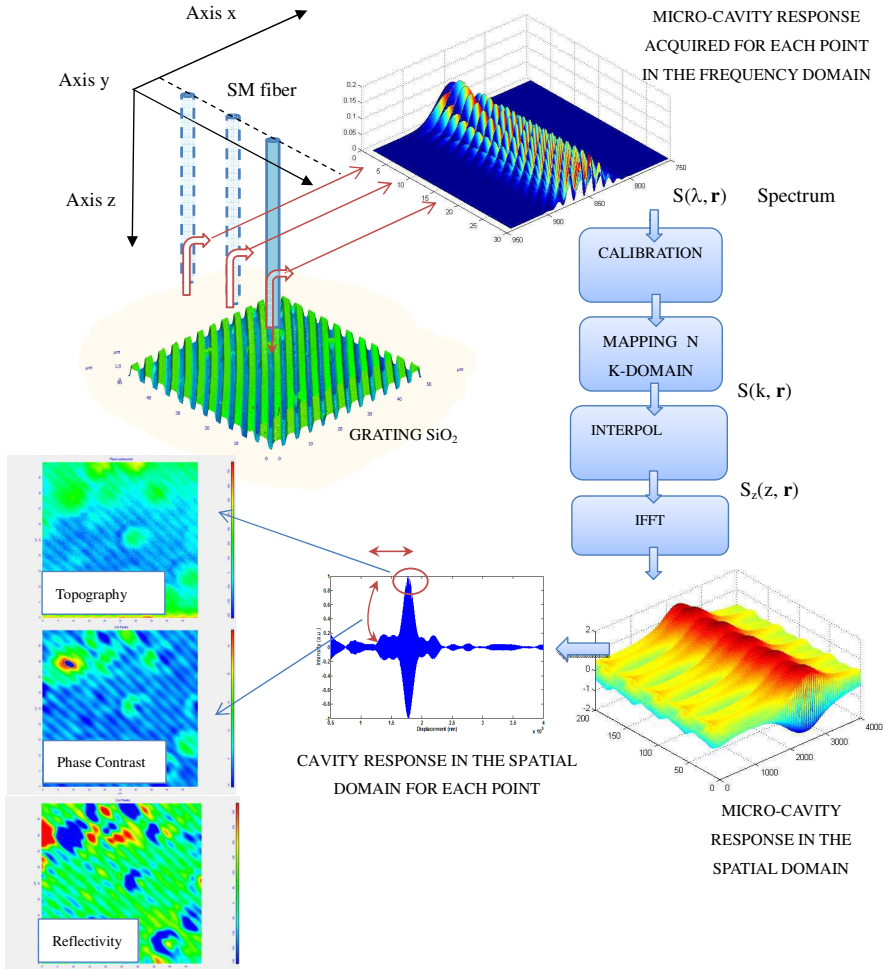
### 3. EXPERIMENTAL SET-UP AND DATA ACQUISITION SCHEME

Figure 3 describes the set-up used to realize the micro-cavity scanning system. A SLED source at 850 nm (bandwidth FWHM = 40 nm) feeds a broad band directional coupler that directs provides separation between transmitted and reflected waves. An addition coupler shifts the wave into a port feeding a photo-detector and a spectrum analyzer. The latter is split by a further coupler that directs the signal to a photo-detector and an Optical Spectrum Analyzer (OSA). The OSA is a high-resolution USB spectrometer with a bandwidth ranging from 650–1080 nm. Combining the spectral range of its grating with the number of detectors and the pixel resolution, it allows an optical resolution of about 0.23 nm. The sample is placed on a piezo-scanner that controls the position with nanometric resolution in the plane and in the normal direction. The cleaved fiber (Numerical Aperture = 0.10–0.14, Mode Field Diameter =  $5.6\ \mu\text{m}$ ) is mounted on a fixed head. The piezo approaches the sample to the fiber making a cavity with a dimension of tens of microns. The current detected by the diode is used as feedback for the scanner, allowing to work in a constant-height mode and to control the position in the plane. For each scanning point intensity and spectrum of the interferometric signal, reflected from the Fabry-Perot cavity, are picked up by the photo-detector and OSA, respectively.

Data acquisition process is described in Fig. 4. Before starting the scan and approaching the cleaved fiber to the sample, the reflected spectrum is measured at a distance in which there is no interaction between fiber facet and sample. These data are used to calibrate, as in Spectral Optical Radars [14], each spectrum acquired.



**Figure 3.** Experimental set-up of the fiber optic micro-cavity scanning microscope.



**Figure 4.** Data acquisition scheme.

Calibration allows to reduce the effects of spurious reflections, rising up in each junction of the fiber path, and the shape of broadband source, both affecting time domain response, mainly for small cavity dimensions. The fiber is then approached to the sample until cavity height is few tens of microns and the interaction with the sample starts to be relevant showing interferences in the shape of the SLED. The spectrum acquired by the OSA in the wavelength domain is mapped to the spatial frequency domain, interpolated by a polynomial algorithm and transformed into time/spatial domain. Following this method and

using the model described in Section 3, we can describe the behavior of the micro-cavity, and in particular changes of the peak-amplitude and peak-position of the spatial domain response, due to variations of the fiber-sample distance and surface permittivity. Data reported in Fig. 4 are simulated assuming the same wavelength resolution as the OSA and following the algorithm described in Fig. 3. We have to point out that, having a fixed wavelength resolution, longer cavity dimension would need higher resolution and sampling frequency of the spectrum.

Figure 5(a) shows the non-linear trend that describes the variation of the peak-amplitude response of the cavity in the spatial domain, when the cavity dimension and the refractive index of the homogeneous sample are changed. For the refractive indexes considered, its

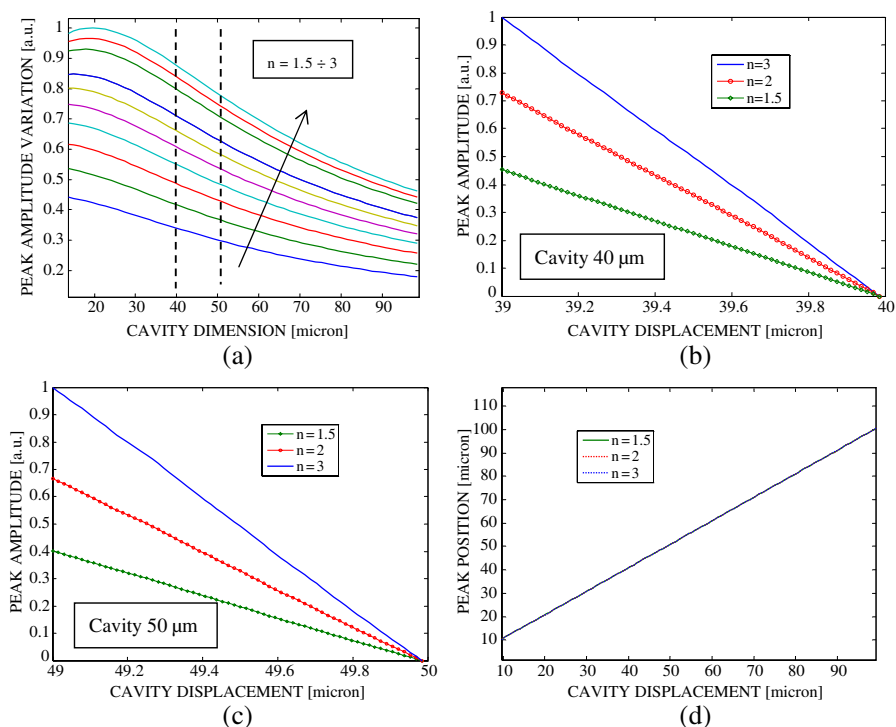


**Figure 5.** Behavior of the peak of the cavity response computed in the spatial domain. (a) Peak-amplitude variation versus the cavity dimension and sample refractive index. (b) The variations are reported for small displacements around 40 μm and (c) 50 μm (the results are normalized and shifted). (d) Shift of the peak for different refractive indices of the sample.

behavior recalls the fringe contrast behavior of the extrinsic fiber optic interferometric signals. The curve in Fig. 5(a) shows the maximum gradient occurs at 40–50  $\mu\text{m}$ , however, for smaller displacements, the peak-amplitude response changes almost linearly, depending on the sample permittivity and cavity dimension as well, (see Figs. 5(b)–(c)). On the other hand, the analysis of peak position (that is how the maximum is displaced) as the cavity size changes, which can be seen with an optical resolution of 0.25 nm, allows to evaluate the cavity dimension, independently from the permittivity of the sample surface.

In Fig. 6, we report the interfering spectra in the frequency domain. In detail, we have compared two spectra acquired at different fiber-surface distances (Fig. 6(a)) and a sequence of spectra profiles acquired in a range of 1 micron surface displacement (Fig. 6(b)), showing a bi-dimensional interfering pattern. A change in the micro-cavity height alters the contrast and frequency of interfering spectrum, as analytically described by (10).

The actual resolution of the system along the normal direction depends on different factors, such as the laser source bandwidth and fluctuations or the piezo-scanner drift that affects the scans in the constant height mode; however, a polynomial interpolation of the spectrum in the  $k$ -domain can provide a theoretical improvement of resolution in  $z$ -direction [9]. A quantitative measure of the root mean square error related to height measurements can be assessed by means of a zero scan area, as usually done in the AFM measurements to estimate environmental noise. In our system, with a 50  $\mu\text{m} \times 50 \mu\text{m}$  scanner the r.m.s. error obtained was about 68.1 nm.

A different consideration must be done for the evaluation of the

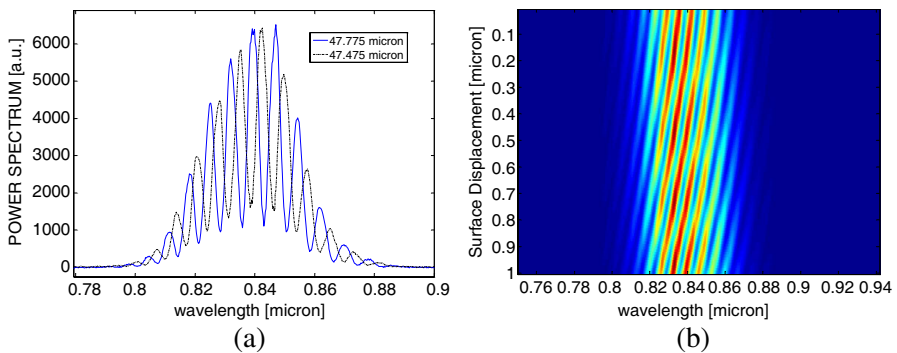


**Figure 6.** (a) Acquired spectra at different fiber-surface distances (continuous line) cavity height = 47.775  $\mu\text{m}$ , (dashed line) cavity height = 47.475  $\mu\text{m}$ . (b) Sequence of spectra acquired by changing the micro-cavity dimension in a range of 1 micron (step = 10 nm).

transverse resolution. Starting from the general definition of resolution, based on capability to distinguish two point objects, it follows that, in a diffraction limited system, it can be defined by overlapping the Airy disks generated at the focal plane. In this case, transverse resolution is not defined through the numerical aperture  $NA$  of the fiber, and consequently, through Rayleigh limit (about  $0.6\lambda/NA$ ). Being the resolution in the plane limited by the diffraction of the electromagnetic field, the in-plane resolution can be evaluated by analyzing the transverse distribution of the electromagnetic field inside the microcavity over the sample surface. To model diffraction effects of the guided mode at fiber facet and fiber-sample interaction, we can use (9), which describes the continuous spectrum of diffracted cylindrical plane waves in  $k$ -space. In Fig. 7(c), we report the transverse electromagnetic power distribution evaluated in spatial domain for different heights.

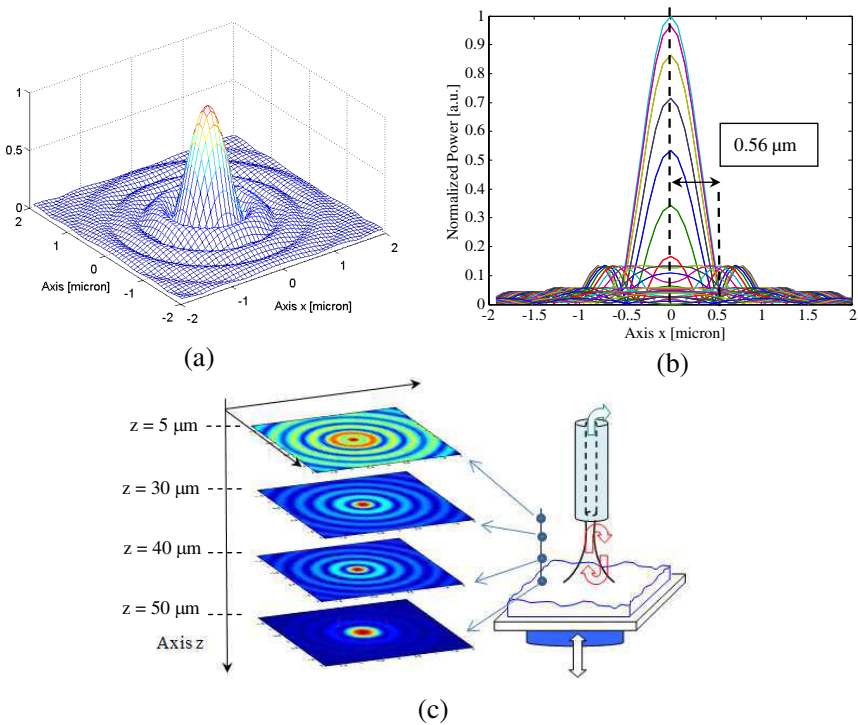


**Figure 7.** Transverse electromagnetic power distribution. (a) Normalized intensity on the sample surface. (b) Power distribution profile. (c) Simulated transverse intensity distribution in 50 μm cavity with a SiO<sub>2</sub> sample.

Intensity distribution of the field along the cavity is a combined effect of diffraction of the field at fiber aperture and the multiple-interferences arising inside the cavity. Interferences shape the field distribution in the time domain and the spot on the sample is characterized by a smaller transverse field distribution than the fiber mode diameter, whereas at different heights over the surface, the power is more spread in the transverse plane. Performing this evaluation when fiber-sample distance is  $50\ \mu\text{m}$ , we obtain that the energy distribution has a radius of the central disk equal to  $0.56\ \mu\text{m}$ , against a fiber mode field radius equal to  $2.3\ \mu\text{m}$ . The transverse resolution can be assumed as the distance of the first null of Gaussian shape from its peak.

The level of signal coupled back in fiber depends on sample reflectivity, absorption and surface scattering. In our micro-cavity scanning system, images are obtained through a Fourier Domain (FD) analysis of the interference signals. As in all FD-based-sensors, the light reflected or scattered back from each point of surface contributes to the interference signal during all the measuring time. This feature makes the system more sensitive and affects the measurable power  $P$  of the signal that is used to extract topographic and contrast phase information. The ratio between the maximum and minimum measurable power of the signal from the surface, defines the dynamic range of the system [25]:

$$\text{DFD} = 10 \log \left[ \frac{4}{\text{SNR}_F^2} \cdot \left( \frac{P_0 t \eta}{h\nu} \right) \right] \quad (13)$$

where  $\text{SNR}_F$  is the minimal necessary signal-to-noise-ratio,  $P_0$  is the total power from the surface,  $h\nu$  is the energy of one photon and  $\eta$  is the quantum efficacy of the photodiode. The more photons from the object contribute to the interference signal, the higher is dynamic range. As shown in [25], for the FD sensors the main physical limitation of dynamic range is the shot noise. In principle, for FD sensors, dynamic range can be greater than typically 14 dB [25]. However, this feature could also make the system more sensitive to other noise sources, as environment vibrations, or moving scatters, etc..

#### 4. EXPERIMENTAL RESULTS

Measurements were performed over Atomic Force calibration gratings whose surfaces have good reflectivity at the working wavelength of 850 nm. The grating is realized in  $\text{SiO}_2$  with a step height equal to  $535 \pm 4\ \text{nm}$ , and a period of  $3.00 \pm 0.01\ \mu\text{m}$ .

Figure 8(a) reports the sample topography acquired by means of an Atomic Force Microscope, whereas Fig. 8(b) shows the topography

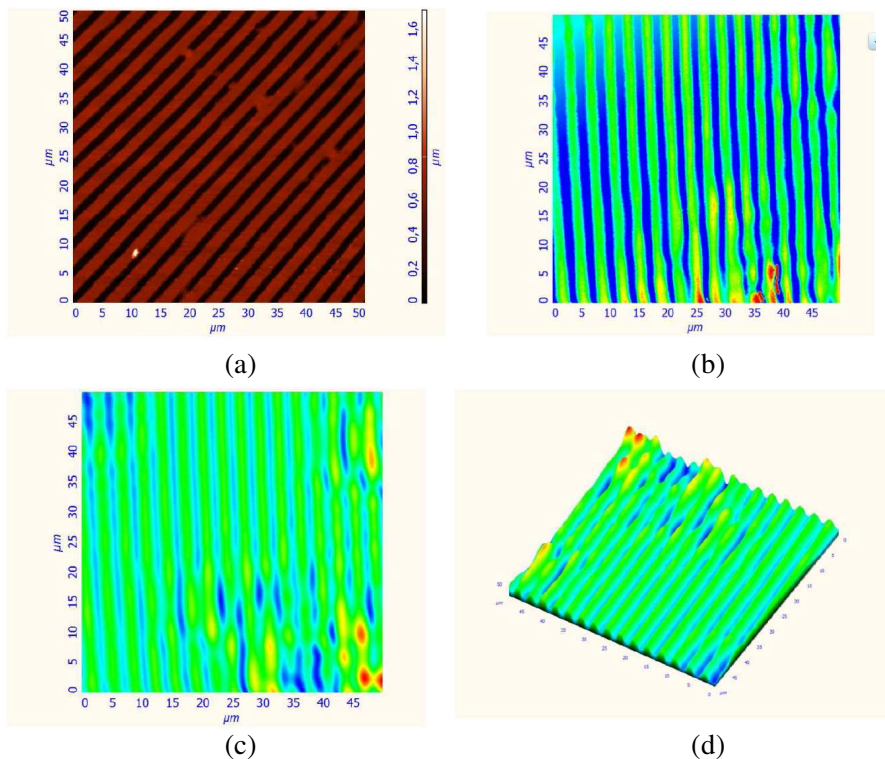


**Figure 8.** Imaging of SiO<sub>2</sub> grating by means of AFM and fiber optic scanning system. (a) SiO<sub>2</sub> calibration grating topography by AFM. (b) SiO<sub>2</sub> grating topography acquired by optical micro-cavity at 850 nm. (c) Contrast phase image. (d) 3D profile of the contrast phase image.

imaged by the micro-cavity scanning system. The images were acquired in different areas and with different grating orientations (cavity dimension = 140 μm).

The topographic profiles acquired by means of the two scanning techniques are compared in Fig. 9. The root mean square of the profiles, gives the level of accuracy in the  $z$ -direction. The AFM curve has an r.m.s value equal to 537,250 nm, whereas the fiber optic scanning system about 529,975 nm. Data highlight the filtering effects, at the higher spatial frequencies, of the single mode fiber with numerical aperture  $NA$ . As described in Fig. 7, the diffracted waves interfere inside the cavity producing Airy disks. According to this transverse pattern, the minimum distance  $d_{\min}$  at which two adjacent points can

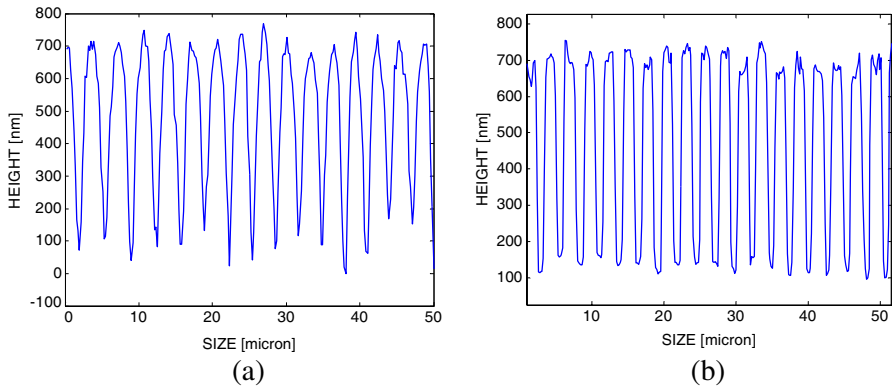


**Figure 9.** Topographic profile of the  $\text{SiO}_2$  grating acquired by (a) fiber optic scanning system and (b) AFM.

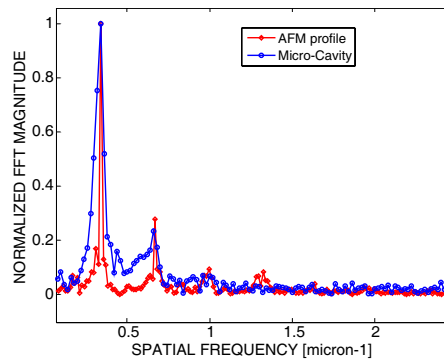


**Figure 10.** Normalized fourier transform magnitude for the topographic profiles reported in Figs. 7(a)–(b).

be resolved is about  $1.12 \mu\text{m}$ ; Limited transverse resolution affects the filtering bandwidth of the optical system as reported in Fig. 10 in which normalized spatial frequencies are compared. The difference between two spectra is more prominent above  $1 \mu\text{m}^{-1}$ , confirming the theoretical value obtained from  $d_{\text{min}}$ , that fixes the bandwidth to about  $0.9 \mu\text{m}^{-1}$ .

The analytical model reported in Section 3 describes how the fluctuations of peak-amplitude response in time domain, produce contrast phase images that are correlated to the sample topography and refractive index changes. Fig. 11 describes the different features that a phase imaging (see Fig. 11(a)) can single out, compared with

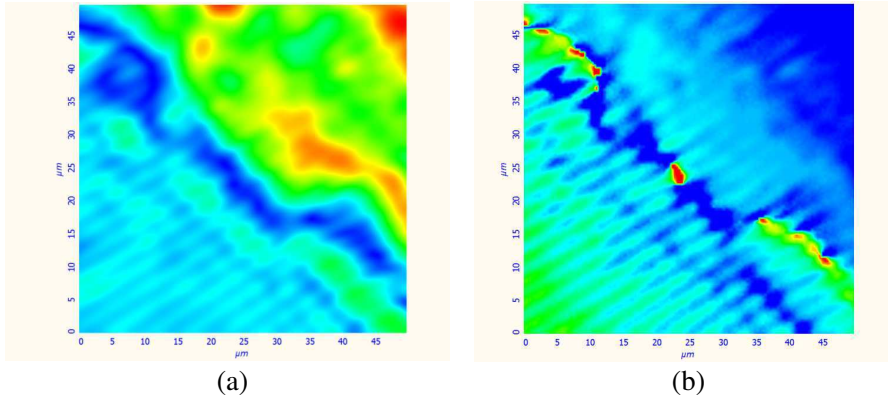


**Figure 11.** SiO<sub>2</sub> grating with a step height equal to  $108.5 \pm 2$  nm having a region contaminated. Differences between the (a) contrast phase and (b) topography images.

the topography image, acquired on the same area (see Fig. 11(b)). The sample is a SiO<sub>2</sub> grating in which part of the surface is contaminated by some impurities. The grating was exposed to open air and actually we do not know exactly what is the source of these impurities. Fig. 10 shows how the presence of very small refractive index changes can give large effects in the phase images, being the phase more sensitive to these variations.

## 5. CONCLUSIONS

In this work, we analyzed and realized an extrinsic micro-cavity scanning system in optical fiber for surface imaging, providing a model for the analysis, which gives information about reflectivity, topography and contrast phase images of the sample. Transverse resolution is defined through the transverse distribution of the electromagnetic field inside the cavity, allowing to overcome the Rayleigh limit. In the normal direction, the resolution although being function of the source bandwidth, can be numerically improved by means of polynomial interpolation. This system has a wide area of applications due to its capability to study topography and contrast phase variations of a sample. Phase imaging measures optical thickness variations due to small changes in refractive index. Different values of refractive index are associated to differences in material density and very small refractive index changes can show a large effects in the phase images. For these reasons, the micro-cavity scanning microscopy could find

application in biomedical field; namely in the characterization of surface roughness and permittivity changes of a cell or tissue, also in liquid environment. The advantage with respect to a near field approach is the reduced interaction with the sample: in particular this aspect can be relevant in biology. In fact, most biologists complain about scanning probe techniques to be too invasive; for example contact AFM flattens samples, or STM expose samples to an external bias etc. Even near field optical approaches usually need some other feedback system based on a strong probe sample interaction. Hence the proposed approach is meant to fill the distance between purely optical microscopes and near field scanning probes.

## REFERENCES

1. Yu, B., et al., "Analysis of fiber Fabry-Pérot interferometric sensors using low-coherence light sources," *IEEE Journal of Lightwave Technology*, Vol. 24, No. 4, 1758–1767, Apr. 2006.
2. Murphy, K. A., M. F. Gunther, A. Wang, R. O. Claus, and A. M. Vengsarkar, "Extrinsic Fabry-Pérot optical fiber sensor," *Proc. 8th Opt. Fiber Sens. Conf.*, 193–196, 1992.
3. Furstenuau, N., M. Schmidt, H. Horack, W. Goetze, and W. Schmidt, "Extrinsic Fabry-Pérot interferometer vibration and acoustic systems for airport ground traffic monitoring," *Proc. Inst. Elect. Eng. — Optoelectron*, Vol. 144, No. 3, 134–144, 1997.
4. Wang, A., H. Xiao, J. Wang, Z. Wang, W. Zhao, and R. G. May, "Self-calibrated interferometric-intensity-based optical fiber sensors," *IEEE Journal of Lightwave Technology*, Vol. 19, No. 10, 1495–1501, 2001.
5. Yao, H.-Y. and T.-H. Chang, "Experimental and theoretical studies of a broadband superluminality in Fabry-Perot interferometer," *Progress In Electromagnetics Research*, Vol. 122, 1–13, 2012.
6. Costa, F. and A. Monorchio, "Design of subwavelength tunable and steerable Fabry-Perot/leaky wave antennas," *Progress In Electromagnetics Research*, Vol. 111, 467–481, 2011.
7. Han, M., Y. Zhang, F. Shen, G. R. Pickrell, and A. Wang, "Signal-processing algorithm for white-light optical fiber extrinsic Fabry-Perot interferometric sensors," *Optics Letters*, Vol. 29, No. 15, 1736–1738, Aug. 2004.
8. Chen, J. H., J. R. Zhao, X. G. Huang, and Z. J. Huang, "Extrinsic fiber-optic Fabry-Perot interferometer sensor for refractive index measurement of optical glass," *Applied Optics*, Vol. 49, No. 29, 5592–5596, Oct. 2010.

9. Zhou, X. and Q. Yu, "Wide-range displacement sensor based on fiber-optic Fabry-Perot interferometer for subnanometer measurement," *IEEE Sensors Journal*, Vol. 11, No. 7, 1602–1606, Jul. 2011.
10. Zhang, Y., H. Shih, K. L. Cooper, and A. Wang, "Miniature fiber-optic multicavity Fabry-Perot interferometric biosensor," *Optics Letters*, Vol. 30, No. 9, 1021–1023, May 2005.
11. Wilkinson, P. R. and J. R. Pratt, "Analytical model for low finesse, external cavity, fiber Fabry-Perot interferometers including multiple reflections and angular misalignment," *Applied Optics*, Vol. 50, No. 23, 4671–4680, Aug. 2011.
12. Kilic, O., M. J. F. Digonnet, G. S. Kino, and O. Solgaard, "Asymmetrical spectral response in fiber Fabry-Pérot interferometers," *IEEE Journal of Lightwave Technology*, Vol. 27, No. 24, 5648–5656, Dec. 2009.
13. Daniels, D. J., *Ground Penetrating Radar*, 2nd Edition, IET, London, 2007.
14. Bouma, B. and G. Tearney, *Handbook of Optical Coherence Tomography*, Marcel Dekker, 2002.
15. Isikman, S. O., et al., "Lensfree on-chip microscopy and tomography for biomedical applications," *IEEE Journal of Selected Topics in Quantum Electronics*, Vol. 18, No. 3, 1059–1072, May–Jun. 2012.
16. Di Donato, A., M. Farina, A. Morini, G. Venanzoni, D. Mencarelli, M. Candeloro, and M. Farina, "Using correlation maps in a wide-band microwave GPR," *Progress In Electromagnetics Research B*, Vol. 30, 371–387, 2011.
17. Farina, M., et al., "Disentangling time in a near-field approach to scanning probe microscopy," *Nanoscale*, Vol. 3, No. 9, 3589–3593, Sep. 2011.
18. Farina, M., et al., "Algorithm for reduction of noise in ultra-microscopy and application to near-field microwave microscopy," *IET Elect. Lett.*, Vol. 46, No. 1, 50–52, Jan. 2010.
19. Kaklamani, D. I., "Full-wave analysis of a Fabry-Perot type resonator," *Progress In Electromagnetics Research*, Vol. 24, 279–310, 1999.
20. Poularikas, A., *The Transform and Application Handbook*, 2nd Edition, CRC Press, 1999.
21. Lee, D. L., *Electromagnetic Principles of Integrated Optics*, John Wiley & Sons, 1986.
22. Ramo, S., J. R. Whinnery, and T. van Duzer, *Fields and Waves*

- in Communication Electronics*, John Wiley & Sons, 1994.
23. Di Donato, A., et al., "Stationary mode distribution and sidewall roughness effects in overmoded optical waveguides," *IEEE Journal of Lightwave Technology*, Vol. 28, No. 10, 1510–1520, 2010.
  24. Di Donato, A., L. Scalise, and L. Zappelli, "Noncontact speckle-based velocity sensor," *IEEE Transactions on Instrumentation and Measurement*, Vol. 53, No. 1, 51–57, 2004.
  25. Andretzky, P., et al., "Optical coherence tomography by 'spectral radar,' dynamic range estimation and in vivo measurements of skin," *Proc. SPIE 3567, Optical and Imaging Techniques for Biomonitoring IV*, Vol. 78, Feb. 1999.